ACADEMIC PRESS

Available at www.ComputerScienceWeb.com
POWERED BY SCIENCE DIRECT®

Computer Vision and Image Understanding 89 (2003) 226–251

Computer Vision and Image Understanding

www.elsevier.com/locate/cviu

An integrated range-sensing, segmentation and registration framework for the characterization of intra-surgical brain deformations in image-guided surgery

Michel A. Audette,[a,*] Kaleem Siddiqi,[b] Frank P. Ferrie,[b] and Terry M. Peters[c]

[a] *National Institute for Advanced Industrial Science and Technology-AIST, Namiki 1-2, Tsukuba 305-8564, Japan*

[b] *Center for Intelligent Machines, McGill University, Montreal, Canada*

[c] *Imaging Research Laboratories, Robarts Research Institute, University of Western Ontario, London, Ont., Canada*

Received 31 January 2002; accepted 15 October 2002

Abstract

Image-guided surgery (IGS) is a technique for localizing anatomical structures on the basis of volumetric image data and for determining the optimal surgical path to reach these structures, by the means of a localization device, or probe, whose position is tracked over time. The usefulness of this technology hinges on the accuracy of the transformation between the image volume and the space occupied by the patient anatomy and spanned by the probe. Unfortunately, in neurosurgery this transformation can be degraded by intra-surgical brain shift, which often measures more than 10 mm and can exceed 25 mm. We propose a method for characterizing brain shift that is based on non-rigid surface registration, and can be combined with a constitutively realistic finite element approach for volumetric displacement estimation. The proposed registration method integrates in a unified framework all of the stages required to estimate the movement of the cortical surface in the operating room: model-based segmentation of the pre-operative brain surface in magnetic resonance image data, range-sensing of the cortex in the OR, range–MR rigid transformation computation, and range-based non-rigid brain motion estimation. The brain segmentation technique is an adaptation of the surface evolution model. Its convergence to the brain boundary is the result of a speed term restricted

* Corresponding author.
E-mail address: m.audette@aist.go.jp (M.A. Audette).

1077-3142/03/$ - see front matter
doi:10.1016/S1077-3142(03)00004-3

to white and grey matter voxels made explicit by a classifier, and the final result is post-processed to yield a *Closest Point Map* of the brain surface in MR space. In turn, this Closest Point Map is used to produce the homologous pairs required to determine a highly efficient, 2D spline-based, Iterative Closest Point (ICP) non-rigid surface registration. The baseline for computing intra-operative brain displacement, as well as the initial starting point of the non-rigid ICP registration, is determined by a very good rigid range–MR transformation, produced by a simple procedure for relating the range coordinate system to that of the probe, and ultimately to that of the MR volume.

1. Introduction

1.1. Preliminaries: image-guided surgery

Image-guided surgery (IGS) describes a class of techniques for localizing anatomical structures on the basis of volumetric image data and for determining the optimal surgical path to reach these structures. With the advent of tomographic image volumes produced by computed tomography (CT) and magnetic resonance (MR), it has become possible to elaborate a 3D image model of the patient, whose internal coordinate system (''*image space*'') can be related to that of a *localization device* spanning the physical space occupied by the patient (''*patient space*''). Brain IGS applications include the treatment of movement and convulsive disorders and of arteriovenous malformations as well as the biopsy, surgical resection, radiotherapy, and brachytherapy of tumours (for a survey see [46]).

The image model typically consists of the tomographic volume itself, displayed in tri-planar view format, as illustrated in Fig. 1, and may include triangulated anatomical boundary surfaces identified from the tomographic scan and rendered onto a computer screen. The position of the point of interest within the 3D image model is conveyed on the basis of:

- the choice of tri-planar view of the underlying tomographic data and the position of the cursor overlaid on each plane, as well as
- the position of a rendered virtual pointer overlaid at the appropriate position and orientation on the displayed anatomical surfaces.

There are two broad categories of localization technique, *frame-based* [21] and *frameless* [27,42,58], with the latter increasingly more prevalent and illustrated in Figs. 1b and c. Frameless localization is generally characterized by a handheld, tracked pointing device, consisting of a *probe* and perhaps a *probe-holder*, whose coordinates are calculated with respect to a reference object, which is generally affixed to a Mayfield clamp immobilizing the head. Assuming that the geometry relating the probe tip to the probe holder is known, and *following a registration procedure that maps image space to the physical space spanned by the tracked probe*, *the anatomical position of the probe tip is reflected by that of the 3D image cursor at all times*. Frameless localization also uses landmarks for determining the image-patient transformation which are extrinsic to the localization device; i.e., fiducials glued to the scalp or imbedded in the cranium.

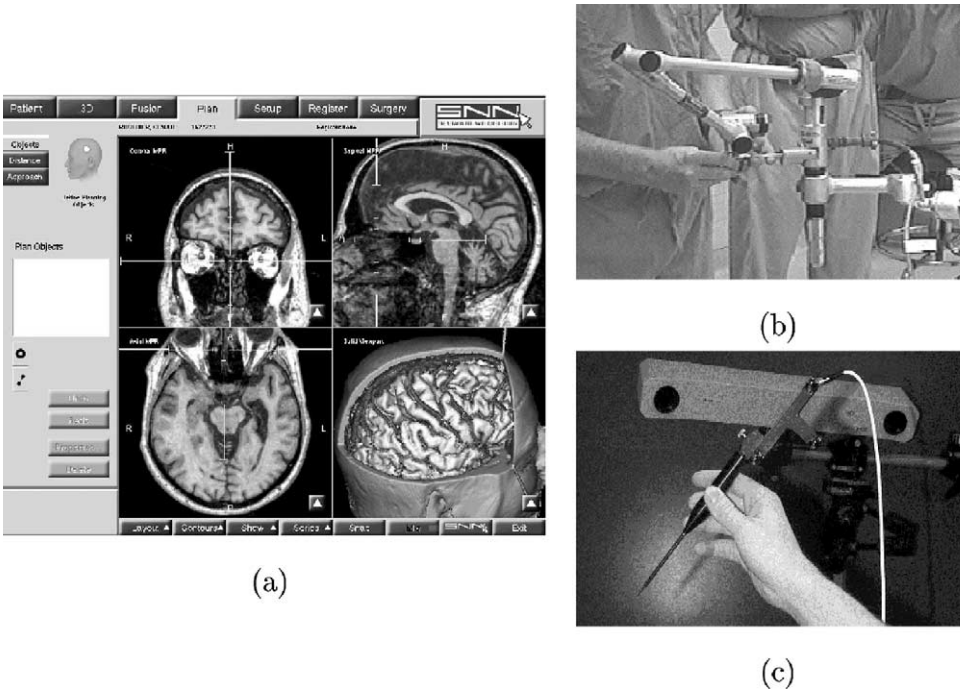

Fig. 1. Image-guided surgery: (a) 3D image model of patient as presented in typical commercial IGS system, namely in tri-planar and 3D view formats, courtesy of Lahbib Soualmi of the Montreal Neurological Institute; frameless localization devices: (b) the FARO arm, during probe calibration, and (c) the Northern Digital Polaris optical tracking system.

The usefulness of image-guided surgery hinges on the accuracy of the transformation between the image and patient spaces. This accuracy is dependent on two conditions:

- first, an accurate initial registration, which in turn presumes accurate tracking equipment [28,44], distortion-free MR/CT data [39], and accurate and consistent fiducial localization [21,38,58],
- and second, a static relationship between patient and image model.

The most important source of error in IGS is the violation of the assumption of static anatomy, *caused by intra-surgical brain shift*. The amount of intra-surgical brain shift, as documented by numerous authors [36,43] often measures more than 10 mm and can exceed 25 mm, and can be ascribed to "the progressive sinking and displacement of the cortical surface as a result of cortico-spinal fluid drainage and progressive mesial displacement of the brain due to gravity" [43].

Existing methods for characterizing brain shift in general exploit either a combination of *sparse* cortical surface displacement data and biomechanical model [37,40], or a combination of volumetric displacement information from tomographic data, namely intra-operative ultrasound [16] or MRI [20], with some form of volumetric

interpolation. Several authors have proposed realistic finite element (FE) [20,40] or mass-spring [49] models of the brain.

1.2. A new approach to estimating brain shift

In this paper, we propose a method for characterizing brain shift that is based on non-rigid surface registration, and can be combined with a constitutively realistic finite element approach for volumetric displacement estimation [20,40,49]. As shown in Fig. 2, our registration method integrates in a unified framework all of the stages required to estimate the movement of the cortical surface in the operating room (OR):

- semi-automatic identification (segmentation) of relevant anatomical surfaces within the MRI volume;
- range-sensing of the exposed brain surface in the OR;
- computation of the range–MRI transformation, based on a calibration procedure and sensor base tracking; and
- non-rigid motion tracking, over time, of the range image of the brain.

Our philosophy for characterizing brain shift is based on the *fast* acquisition and processing of *dense* displacement information, using a sensor that could easily be deployed to, and retracted from, a scanning position, with an appropriate mounting framework. This perspective is dictated by the spatially and temporally under-determined nature of non-rigid motion estimation. In addition, the semi-automatic surface identification stage presented here can be explicitly integrated with meshing software to make a finite element model *patient-specific* with little user interaction. Finally, a range-sensor is less expensive than both ultrasound and intra-operative MR, as well as easier to use.

Our brain segmentation technique is an adaptation of surface evolution models [12,34]. Its convergence to the brain boundary is the result of a speed term restricted to white and grey matter voxels made explicit by a classifier [18], and the final result

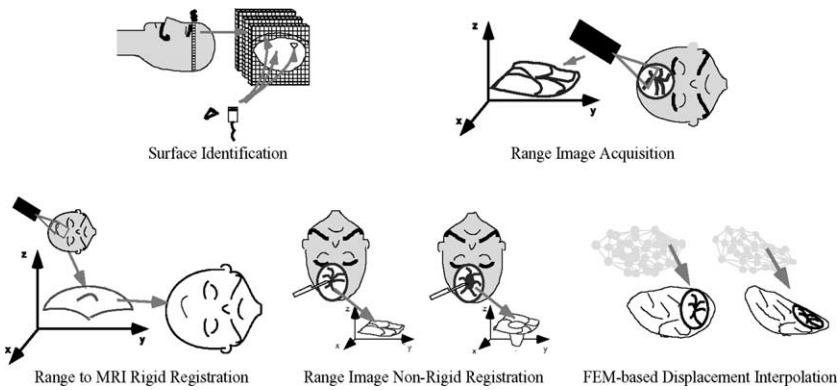

Fig. 2. Brain shift estimation framework, featuring the four stages comprising our non-rigid surface registration framework, which can be combined with a FE-based volumetric displacement estimation stage.

is post-processed to yield a Closest Point Map of the brain surface in MR space. In turn, this Closest Point Map is used to produce the homologous pairs required to determine a highly efficient, 2D spline-based, Iterative Closest Point (ICP) [8,30] non-rigid surface registration. In particular, given an initial range–MR transformation, this Map associates with each MR voxel the label of its closest brain surface point, so that for any transformed cortical range point coinciding with that voxel, its closest MR homologue is immediately looked up. Finally, the baseline for computing intra-operative brain displacement, as well as the initial starting point of the non-rigid ICP registration, is determined by a very good rigid range–MR transformation, produced by a simple procedure for relating the range coordinate system to that of the probe, and ultimately to that of the MR volume. For a survey of anatomical surface registration techniques, the reader is referred to [4].

The rest of this paper presents details of our method for computing the brain surface displacement as follows. Section 2.1 examines how laser-based range-sensing can provide 3D brain shape data in the operating room, as well as presents our procedure for computing the rigid transformations which relates the range coordinate system with the probe and MR coordinates systems. Next, the non-rigid registration of a time sequence of range images of the brain, to estimate the intra-surgical cortical surface displacement over time, is the subject of Section 2.2. Finally, the identification of the cortex in the MR volume is addressed in Section 2.3. This section discusses our contributions to making surface evolution models better adapted to identifying the brain surface and to post-processing the brain surface in order to improve the efficiency of the subsequent registration with range data. Our validation study and a discussion of each stage is then presented in Section 3.

2. Materials and methods

2.1. Laser range-sensing and calibration-based range–MR transformation

In order to characterize brain shift, one must first find a simple-to-use, robust means of measuring the 3D shape of the brain exposed in the OR. We have chosen to measure the external surface shape, rather than use a tomographic method, because of the ease of use of a surface tracking and FE approach. Moreover, tomographic studies have indicated that much of the brain movement is concentrated near the brain surface exposed by the craniotomy [15,36], so that a good characterization of the volumetric displacement function is possible with a surface tracking and FEM approach. Even in the presence of deep structure motion, our assumption is that brain shift is not discontinuous over brain depth, that the combination of surface motion and of a realistic biomechanical model (in both constitutive properties and boundary conditions) will accurately predict this motion, and that the effect of tissue resection can be assessed independently [48].

Laser-based range-sensing is the industrial standard for quickly and accurately acquiring dense, quantitative information on 3D shape. Fig. 3a illustrates the dense shape characterization of the cortical surface achievable with this technology. It is

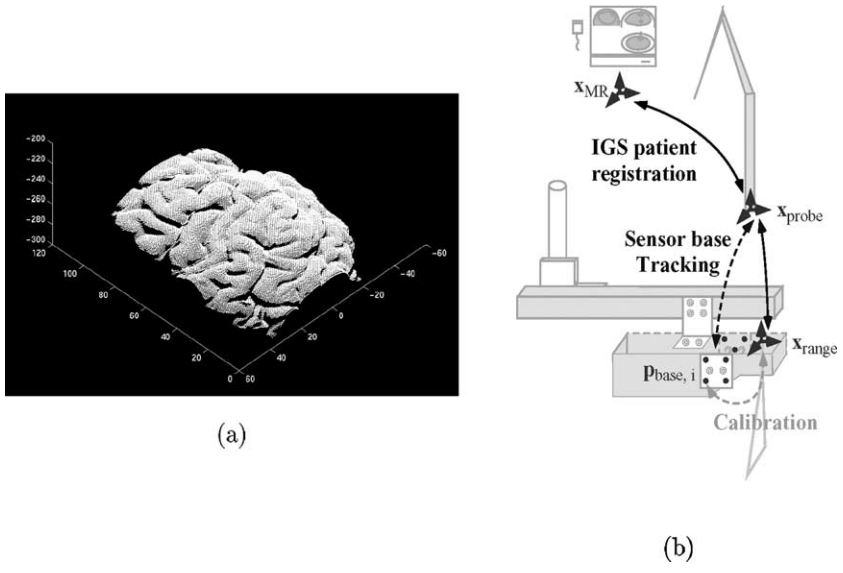

Fig. 3. (a) Range image of the left hemisphere of a human brain. (b) Range to MR transformation geometry, illustrating the range, probe, and MR referentials and the sequence of procedures for relating them to each other.

worth noting that other 3D surface shape estimation methods could have been used, such as shape-from-stereo, particularly if integrated with a binocular surgical microscope. Moreover, there are two registration problems that are relevant to our method for characterizing brain shift: *relating range data to MR data* and *tracking the non-rigid cortical motion over time* implicit in the time sequence of range images. The first problem could perhaps have been solved by computing the MR-range transformation on the basis of a fully autonomous registration of cranial skin surfaces produced by the two modalities. However, our technique, inspired by Comeau's ultrasound-to-MR registration method [16], uses the tracked probe to establish this transformation, as illustrated in Fig. 3b. It features a *calibration* stage that relates the internal range coordinate system to external plates, featuring milled divots, bolted to the range-sensor, a *sensor base tracking* stage that determines the range–probe transformation in the OR, and an *IGS patient registration* stage, whose MR–probe transformation is finally multiplied by the range–probe transformation to relate the range and MR coordinate systems.

2.1.1. Laser range-sensing

The 3D coordinates of the exposed cortical surface are computed by a commercial range-sensor made by Vitana [9,54] (Ottawa, Canada). This sensor uses both laser-based *triangulation* and *defocusing* techniques to estimate range data (for details see [9]). Moreover, it produces a 2D range-map of a "slice" of the surface, along x–z coordinates, with a pixel accuracy of 0.4–0.5 mm along x and of 0.5 mm along z [54]. The sensor is mounted on a commercial linear positioner,

produced by Intelligent Actuator [23], whose position, orthogonal to the range profile, provides the y-coordinate. The regular sampling nature of the sensor CCD and the constant-rate data acquisition along the y-axis result in the collection of uniformly spaced samples, typically on a 256×256 grid. Moreover, a range image can be obtained in a matter of seconds, once the sensor is deployed in scanning position.

2.1.2. A procedure for relating range to MR space

The baseline for cortical movement is implemented by computing the rigid-body transformation between range and MRI spaces and applying this transformation to the identified cortex surface in the scan. In the literature, computing an arbitrarily large transformation between two surfaces is generally approached with features based on the differential geometry of the surfaces [22,52], or global descriptions [11,25] of surface shape. However, an autonomous registration procedure would have to rely on a small skin patch, surrounded by surgical draping, and neither kind of approach would likely be sufficiently discriminating. Our technique uses the IGS tracked probe to establish the position in probe space, and ultimately in MR space, of the *sensor base*, coinciding with a configuration of milled holes in two external plates bolted to the sensor. All that is needed to complete the picture is a *calibration* procedure to relate the sensor base to the sensor internal reference. An important point to be made here is that a very accurate range–MR transformation is achievable from the automatic detection of implanted fiducials [38,55], but we chose to proceed otherwise because of the practice at our institute of not using implantable fiducials.

The geometry of the calibration, sensor base tracking, and IGS registration is seen in greater detail in Fig. 4. The objective of the overall procedure is to find a way to relate range coordinates to MRI coordinates. The goal of the calibration, which can take place outside of the OR and is illustrated in Figs. 4a and b, is to relate the inner range-sensor reference to the milled divots on its outer side-plates, or sensor base. The goal of the sensor base tracking, as shown in Fig. 4c, is to establish the position of these sensor base points in probe coordinates at time t_0 in the OR, and use this information along with the calibration results to relate the inner range-sensor reference to probe space. The probe–image transformation, produced by the IGS patient registration, can then be used to relate range to MR coordinates, as featured in Fig. 4d. To simplify the formalism adopted for this section, we use the letters R, P, and M to designate *range*, *probe*, and *MR* coordinates, while t_c and t_0 correspond to time instants coinciding with *calibration* and the intervention in the *OR*.

The calibration procedure (refer to Fig. 4) consists of the following steps, assuming that the sensor is brought to *home position*, $y = 0$:

1. *Linear positioner calibration*. The y-coordinate is calibrated with a long plate featuring a row of machined divots at a $10 \pm .01$ mm spacing.
2. *Range-sensing of a* "*wedding cake*" *non-coplanar calibration tool*, featuring an array of milled holes of 2 mm radius.
3. *Automatic identification of hemispherical pits* $\mathbf{p}_{T,j}^{R,t_c}$ *within the range image of sensor calibration tool* by *template matching* [45].

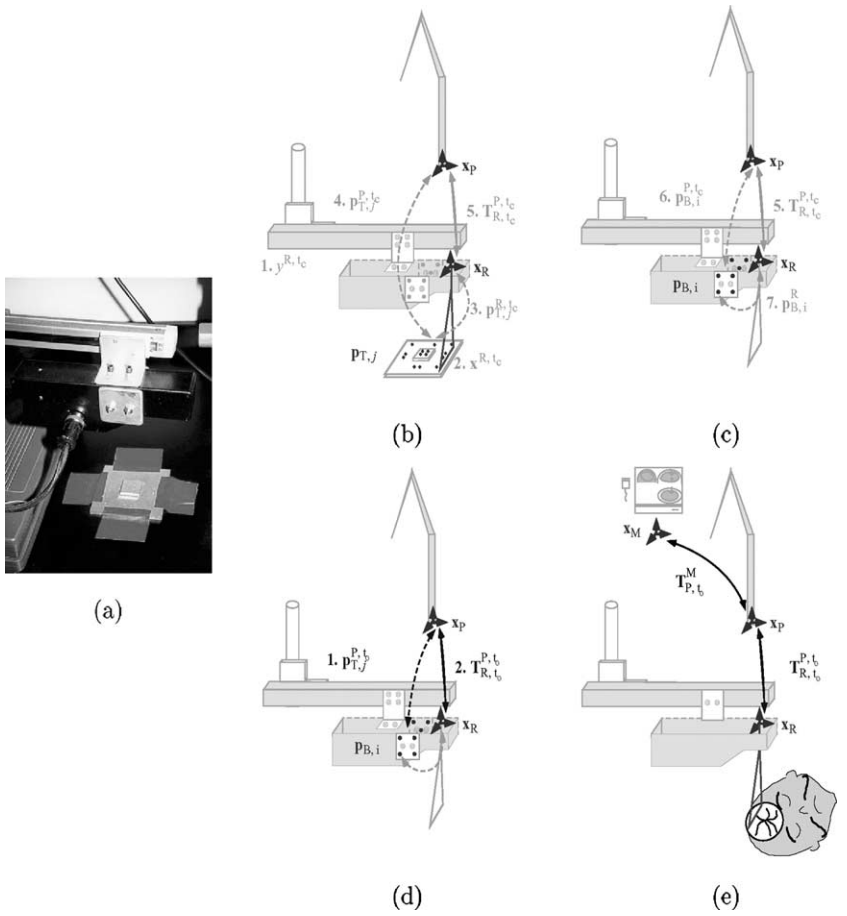

Fig. 4. (a) Range-sensor with calibration tool and external plates (sensor base). (b–d) Range to MRI transformation computation. At $t = t_c$, the calibration procedure first relates range to probe space (b), then determines the sensor base points in range space (c). (d) Sensor base tracking determines sensor base points in probe space at $t = t_0$ and finds the range–probe transformation in the OR. (e) The final step uses this and the probe–MR transformation to map range to MR.

4. *Probe–space identification of pits* in the tool, $\mathbf{p}_{T,j}^{P,t_c}$, by insertion of the probe tip.
5. *Registration of range pits* $\mathbf{p}_{T,j}^{R,t_c}$ *with probe–space coordinates of the pits* $\mathbf{p}_{T,j}^{P,t_c}$, producing a probe–range transformation $\mathbf{T}_{P,t_c}^{R,t_c}$ at time t_c [3].
6. *Probe–space identification of sensor base points*, i.e., the 9 milled divots in the outer side-plates bolted to the sensor: $\mathbf{p}_{B,i}^{P,t_c}$.
7. *Apply probe–range transformation to sensor base points*:

$$\mathbf{p}_{B,i}^{R} = \mathbf{T}_{P,t_c}^{R,t_c}\mathbf{p}_{B,i}^{P,t_c}, \tag{1}$$

relating the sensor base points to the range referential.

The sensor base tracking procedure in the OR at t_0 is as follows:

1. *Identify the location of pits in sensor side-plates in probe space*, to characterize the new sensor base position: $\mathbf{p}_{B,i}^{P,t_0}$.
2. *Match probe–space pits with the points* $\mathbf{p}_{B,i}^{R}$ to determine the probe reference–range transformation $\mathbf{T}_{R,t_0}^{P,t_0}$ for the configuration at time t_0.

Finally, the range data comprising surface S_B are then related to MRI-space anatomical surfaces by considering the IGS probe–MRI and the probe–range transformations:

$$\mathbf{x}_{S_B,t_0}^{M} = \mathbf{T}_{P,t_0}^{M}\mathbf{T}_{R,t_0}^{P,t_0}\mathbf{x}_{S_B,t_0}^{R} = \mathbf{T}_{R,t_0}^{M}\mathbf{x}_{S_B,t_0}^{R}. \tag{2}$$

The final result can be further refined with a rigid-body Iterative Closest Point registration, based on the skin surface identified in MR/CT data, and imaged in the OR by the range-sensor. The sensor base tracking procedure steps 1 and 2 can be performed in less than a minute, together with the range data acquisition, following the deployment of the sensor to a scanning position. The deployment of the sensor, on a locking articulated arm or on a programmable robot, could also be achieved within a minute or so, although the prototype described here was not tested in the OR. A dense 256×256 grid of range points, referred to MR space, is therefore achievable is considerably less time than it takes to manually acquire a sparse, probe-based cloud of cortical surface points.

2.2. Surface non-rigid displacement estimation

2.2.1. Motivation and overview of non-rigid cortical motion estimation

Brain shift at the exposed cortical surface, measured with respect to the rigidly transformed pre-operative brain surface identified in MRI, can be characterized as non-rigid surface motion captured by the initial range image, as well as those displacements captured in subsequent range images. This surface motion is estimated with a non-rigid Iterative Closest Point [8,30] registration technique. ICP techniques start from a rough initial alignment between two surfaces S_A and S_B, and iteratively use the set of *closest point pairs* between the two surfaces to determine a new incremental transformation. The incremental transformation $\mathbf{T}_k$ corresponding to the kth iteration is then applied to one of the surfaces (which may already be transformed), namely $\mathbf{T}_{k-1}S_B$, gradually improving its alignment with S_A. In most applications, the transformation $\mathbf{T}_k$ consists of an incremental rotation $\mathbf{R}_k$ and translation $\mathbf{t}_k$.

In our non-rigid registration application, $\mathbf{T}_k$ may also represent a 2D local piecewise polynomial function: a *smoothing surface spline*. The choice of a surface spline-based ICP technique is justified by its suitability to non-rigid motion estimation, in contrast with approaches based on features and global shape. Moreover, this technique is better suited than an active surface model to tracking an open range image [4,5]. The main drawback of such an iterative technique is the requirement of a rough initial alignment, but this is provided by the range–MR transformation procedure.

Prior to providing implementation details of our registration, we present a new elastically deformable brain-shaped [7] validation phantom, as shown in Fig. 5, made

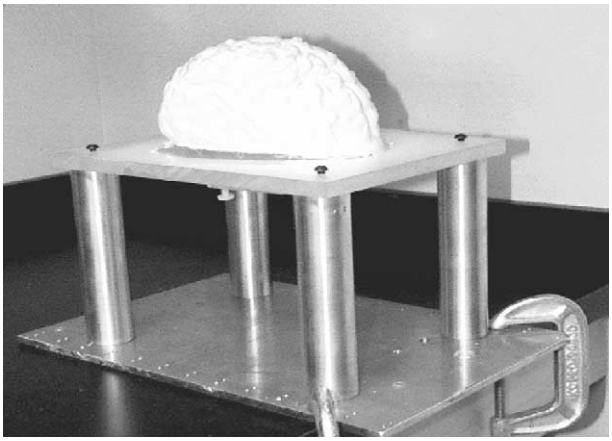

Fig. 5. Elastic PVA-C brain phantom.

from *Polyvinyl Alcohol Cryogel* (PVA-C) [13]. PVA-C is a relatively *viscous liquid*, which upon freezing and thawing, becomes an *elastic solid*. Furthermore, PVA-C can produce material properties comparable to values published in the literature for grey and white matter [57]. This phantom rests on a support plate of plexiglass (usable within an MR scanner), and features a moving assembly consisting of a small disk and rod, also of plexiglass, imbedded within the elastic material. The movement of this imbedded disk, in response to changes in the position of set-screws, triggers material deformation.

2.2.2. ICP homologous pairs by look-up: the Closest Point Map

The iterative registration technique proposed here bears comparison to that of Lavallée and Szeliski [30,50], where the volume spanning one of the surfaces is preprocessed with an octree-based distance map to accelerate its registration with the second surface. When a second surface falls within the mapped volume, each point on it inherits a distance value to its closest homolog of the first surface. Because this preprocessing produces a distance map, but does not provide homologous pairs, the subsequent registration must still resort to an optimization method to determine the best transformation.

In contrast, our method incorporates a processing stage applied to the identified brain surface in the MRI volume, based on a propagative distance-to-surface algorithm called the *Fast Marching* (FM) method [47], and which is modified to produce a *Closest Point Map* [5] as well. The Fast Marching method is used to compute distances from a given surface, such as shown in Fig. 6a for tri-planar images of the elastic brain phantom. The Closest Point Map is an adaptation of this method, whereby the *label of the closest surface point*, from which the distance is computed, is also stored. Moreover, as shown in Section 2.3, the FM method is also used to initialize the surface model with which we identify the outer brain surface. In other

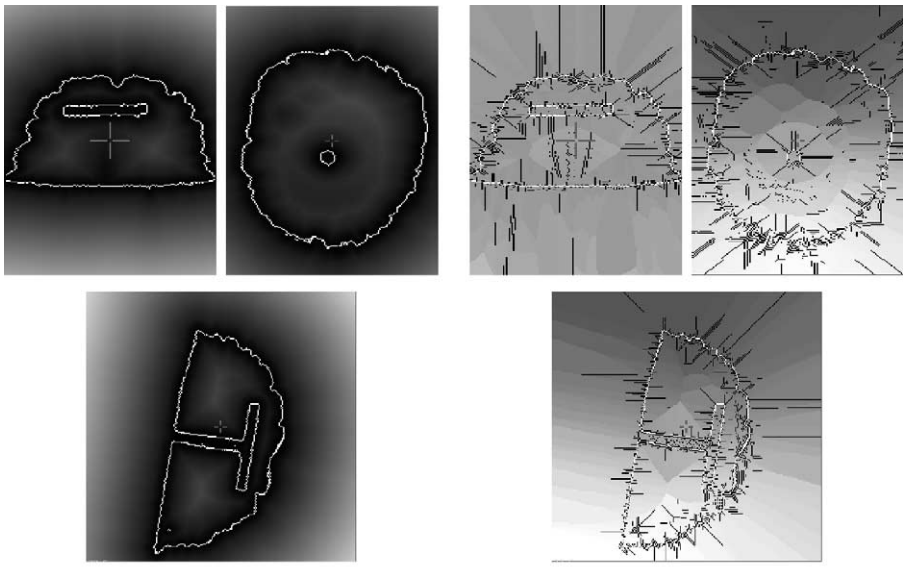

Fig. 6. (a) Distance and (b) Closest Point Maps computed from the surface of the elastic phantom (white), and shown in tri-planar views, mapped to a grey level. In (b) ambiguous voxels, possessing more than one closest surface point, are shown in black.

words, the same numerical estimation framework serves to both improve the efficiency of the registration and to initialize the brain segmentation algorithm. To every voxel in MRI space, the Closest Point Map associates the label of the brain (or phantom) surface point closest to it. This concept is shown in Fig. 6b for tri-planar images of the elastic brain phantom, with labels mapped to a grey-level and with ambiguous voxels (more than one closest point) identified in black.

The characterization of non-rigid motion becomes much more efficient if its starting point is a dense set of homologous pairs, as opposed to a distance map which imposes a costly minimization at each ICP iteration. Each rigid transformation iteration can exploit a closed-form computation method [3], any of which requires explicit point-pairs, not distances between them. Each non-rigid iteration can also make use of a dense vector displacement function obtained by look-up, and as will be seen in the next section, a highly efficient numerical scheme for smoothing this function with surface splines. The justification for emphasizing computational efficiency here is two-pronged: *clinical acceptability* and the inherent *temporal underdetermination* in estimating non-rigid motion.

2.2.3. Modeling non-rigid surface displacement with 2D recursive spline filtering

The regular spacing of the range data is exploited by using extremely efficient *recursive smoothing splines* [53] to smooth the vector displacement field. These surface splines express the fitting of interpolating, smoothing or approximating splines as

recursive filters, provided that the data samples exist at regular positions. As mentioned earlier, this is the case for the range surface points.

For this work, we adopt a smoothing spline approach, whose first stage is a convolution with a smoothing kernel[1]

$$S_{\lambda}^{n}(Z) = 1 \Big/ \left(B_1^n(Z) + \lambda(-Z + 2 - Z^{-1})^{\frac{n+1}{2}} \right), \tag{3}$$

where $B_1^n(Z)$ is the *indirect B-spline transform* given by Unser [53], n is the order of the spline fitting, and λ is the regularization parameter of the smoothing. This stage produces B-spline coefficients and is followed by a convolution with the indirect transform $B_1^n(Z)$ to yield the smoothed output. The filters can simply be cascaded to implement smoothing in 2D. A first-order fit is chosen, i.e., $n = 1$, to limit overshoots due to a higher-order continuity constraint. This first-order recursive IIR filter can be broken down into factors in Z and Z^{-1}, and implemented as separate anti-causal and causal filters, respectively, which translates into local operations involving the *current and immediately neighbouring* pixels, independently of the smoothing parameter λ (for further details, see [53]).

In order to make the non-rigid motion estimation well-behaved, the registration features the following stages:

- A *rigid registration* stage: a series of instantaneous rigid ICP iterations. This stage is halted when the registration error is no longer reduced significantly.
- A *non-rigid registration* stage: a series of non-rigid ICP iterations where the smoothing parameter λ is initially set very high, and is gradually lowered as the process iterates, progressively resolving finer-level motion detail.

2.2.4. Special considerations for range–MR non-rigid surface registration

Each non-rigid registration iteration may require some additional consideration, in comparison to a rigid-body stage. At some pixels in the range-sensor CCD, a low signal can occur, resulting in a gap or an unreliable range point. Such a low signal value can be detected from the z-value or intensity profile of the range image and pruned. Furthermore, because the range data are somewhat denser than the MR-based cortical surface points, the range–MR homologous pairs are *many-to-one*. Consideration of all of the homologous pairs would lead to an erroneous tangential displacement component. This issue suggests refining these many-to-one homologous pairs, resulting in a set of *mutually closest pairs*, followed by a proximity-weighted displacement propagation. In the neighbourhood of gaps, the non-rigid motion estimation is more reliant on this displacement propagation. While it is geometrically feasible for a voxel to have more than one closest surface point, simple disambiguation and validation of each homologous pair are possible, based on the assumption of *continuous displacement* [35]. This test is a comparison between the displacement vector determined by each homologous pair, and an average displacement computed from neighbouring points.

[1] Note: here Z relates to the Z-transform.

Finally, the result of the procedure described so far is a *forward range–MR transformation* $\mathbf{T}_R^M$, composed of a final multiplicative rigid transformation $\mathbf{T}_{R,r}^M$ which is the product of successive ICP transformation matrices,[2] followed by an additive spline-based non-rigid displacement function $\mathbf{T}_{R,n}^M$:

$$\mathbf{x}'_{R,i} = \mathbf{T}_R^M(\mathbf{x}_{R,i}) \equiv \mathbf{T}_{R,n}^M\left(\mathbf{T}_{R,r}^M \mathbf{x}_{R,i}\right),$$
$$\text{where } \mathbf{T}_{R,r}^M = \mathbf{T}_{R,r,K}^M \cdots \mathbf{T}_{R,r,1}^M \text{ and } \mathbf{T}_{R,n}^M(\mathbf{x}) \equiv \mathbf{T}_{R,n,L}^M \cdots \left(\mathbf{T}_{R,n,K+1}^M(\mathbf{x})\right). \tag{4}$$

The indices K and L indicate the final iterations of rigid (multiplicative) and non-rigid (additive) ICP registration. In turn, the following recursive expression further defines the lth non-rigid transformation

$$\mathbf{T}_{R,n,l}^M(\mathbf{x}) \equiv \tilde{\mathbf{d}}_l\left(\mathbf{x} + \tilde{\mathbf{d}}_{l-1}\right) + \mathbf{T}_{R,n,l-1}, \tag{5}$$

where $\tilde{\mathbf{d}}_l$ represents the smoothed displacement at iteration l, evaluated at a transformed range point. In other words, the method described so far maps the range surface data $\{\mathbf{x}_{R,i}$, where $\mathbf{x}_{R,i} \in S_R\}$ to MR space, in a manner that conforms to the pre-operative MR cortical surface data $\{\mathbf{x}_{M,j}$, where $\mathbf{x}_{M,j} \in S_M\}$.

What is needed to characterize brain shift, however, is the *inverse transformation* $\mathbf{T}_M^R$ which non-rigidly maps the pre-operative MR brain surface data $\mathbf{x}_{M,j}$ to conform to the intra-operative cortical range data. The inverse transformation of $\mathbf{T}_R^M$ is the negative of the overall range–MR non-rigid vector displacement field applied to pre-operative MR data, followed by the application of the inverse, or transpose, of the overall range–MR rigid-body transformation:

$$\mathbf{x}'_{M,j} = \mathbf{T}_M^R \mathbf{x}_{M,j} = \mathbf{T}_{M,r}^R \mathbf{T}_{M,n}^R\left(\mathbf{x}_{M,j}\right), \quad \text{where } \mathbf{T}_{M,n}^R(\mathbf{x}) = -\mathbf{T}_{R,n}^M(\mathbf{x}) \text{ and } \mathbf{T}_{M,r}^R$$
$$= \mathbf{T}_{R,r}^{M^{-1}} = \mathbf{T}_{R,r}^{M^T}. \tag{6}$$

The computation of the inverse transformation in this manner pre-supposes the smoothness of the forward non-rigid mapping, in a manner sufficient for the inverse to be well-defined, and the absence of significant occlusions.

2.3. Model-based brain surface segmentation

Currently, the traditional technique for identifying anatomical surfaces in IGS is a labour-intensive slice-by-slice approach where a "seed" is selected, corresponding to the tissue type of interest, and a software program identifies the rest of the contiguous voxels which are of similar intensity [24]. The contiguous labelled voxels within these slices together comprise a volume of interest, coinciding with brain tissue for example, the outer surface of which constitutes the boundary of interest. In contrast, a semi-automatic segmentation technique in general requires far less user interaction, has better reproducibility than a manual approach, can incorporate prior knowledge

[2] Homogeneous coordinates reduce the application of successive rigid body transformations to a sequence of matrix multiplications [17].

into the model to avoid common pitfalls, and can easily process image volume information in a fully 3D manner. Surface models can be categorized into those based on an explicit representation and on a physical equilibrium between virtual internal properties of the model and image-based external forces [26,51], and those based on the evolution of an implicit surface expressed as a partial differential equation in time, which imbeds the problem into one defined over the complete image domain [12,34] (for a survey see [41]). We adopt a surface evolution model because of its topological adaptability and simple formulation in 3D.

2.3.1. Surface evolution model with classifier-based speed term

The anatomical surface identification technique presented here is known as a surface evolution model [12,34], which is characterized by imbedding the identification of a 3D surface $\mathcal{S}$ into the evaluation of a function Ψ whose domain spans the image volume:

$$\{X \in \Re^3 \text{ such that } \mathcal{S}(t) \equiv X : \Psi(X,t) = 0\}. \tag{7}$$

$$\frac{\partial \Psi}{\partial t} = F(x,y,z)\|\nabla\Psi\|\left[\operatorname{div}\left(\frac{\nabla\Psi}{\|\nabla\Psi\|}\right) + v\right] + \nabla F \cdot \nabla\Psi, \tag{8}$$

where $\operatorname{div}(\nabla\Psi/\|\nabla\Psi\|)$ represents the mean curvature H of an isosurface of the function Ψ. This model features a *diffusive* smoothing term $\|\nabla\Psi\|\operatorname{div}(\nabla\Psi/\|\nabla\Psi\|)$, a *hyperbolic* motion term $\|\nabla\Psi\|v$, and two image terms: a *speed* function F and a *doublet* term $\nabla F \cdot \nabla\Psi$ which serve to bind the evolving surface to the anatomical boundary of interest. Moreover, the model is initialized by one or more initial user-defined surfaces $\{\Psi(X,0) = 0\}$ which fully contain, or are fully contained by, the anatomical boundary.

The model evolves in a manner which nudges the zero-level isosurface $\{\Psi(X,t) = 0\}$ inwards or outwards until the image terms bind it to the boundary. The imbedding function Ψ is initialized as a *signed distance map* from the initial user-defined surface(s). For the sake of efficiency, we restrict the computation of our model to a narrow band [1], whereby the model is computed only within a thin volumetric shell close to the evolving $\{\Psi(t) = 0\}$ isosurface. As mentioned earlier, we choose the Fast Marching (FM) technique in order to compute distances from the $\{\Psi(X,t) = 0\}$ isosurface, to initialize $\Psi(X,t)$ over its whole domain and to restrict the computation to a narrow band near the $\{\Psi(X,t) = 0\}$ isosurface.

In most existing implementations of surface evolution models, the speed term is a function of the image gradient, i.e.,

$$F = \frac{1}{1 + \|\nabla\tilde{I}(x,y,z)\|^n}, \tag{9}$$

where typically $n = 1$, 2, or 3 and $\tilde{I}(x,y,z)$ is usually a Gaussian-filtered image (MR) volume. However, this approach has some limitations when it comes to identifying the brain surface, such as a lack of T1 contrast between grey matter and the sagittal sinus and between grey matter and muscle tissue, possibly entailing a bleeding effect outside the brain surface. To alleviate this problem, the model is endowed with

higher-level anatomic information, namely by first running a Minimum Distance (MD) *tissue classification* algorithm [18] on the image volume(s), and to compute a speed function which restricts the surface model to expand only within voxels classified as white matter (WM) and *certain* grey matter (GM) voxels, according to the following discrete relation:

$$\begin{aligned} F(x,y,z) &= 1.0 \quad \text{if } \{(x,y,z) \in WM\} \text{ or } \{(x,y,z) \in GM \text{ and near } WM\}, \\ &= 0 \quad \text{otherwise.} \end{aligned} \tag{10}$$

Other classification techniques were considered, but the MD technique performs well with a small training set (the presence of pathology may preclude warping a large, generic training data set to patient data) and with T1-weighted data alone. Tissue classification is the thrust of ongoing research of ours [6] and is a complex issue in itself, particularly if it must cope with pathological data and with a relatively small set of training points. While it would appear feasible to simply consider the outside surface of GM points (with the Marching Cubes algorithm [31] for example) in practice, false GM positives which are iso-intense with GM (e.g., muscle) do arise and would undermine such an approach, particularly if only T1 data are available. The classifier-based surface model also offers an elegant means of integrating multi-spectral data, such as T1-, T2-, and PD-weighted MR, if available.

2.3.2. Surface model implementation

Our implementation is a two-stage procedure which first identifies the outer WM boundary, then, based on a flexible coupling implemented with the *WM/GM Distance Function* (WDF) [5], the outer brain surface is identified with the position of the WM boundary as a constraint. The effect of this coupling on the speed term computation is illustrated in Fig. 7. One advantage of our method over more rigidly coupled surface models [32,56] is that it will tolerate embedded pathologies. Moreover, the threshold that limits the motion of the brain surface through GM voxels varies according to spherical coordinates, so that the coupling between white and grey matter takes into account prior assumptions about the thickness of grey matter, which is much thinner in the cerebral cortex than in the cerebellum or lower frontal area, for example.

The surface model computation culminates in a post-processing of the outer brain surface to produce a *Closest Point Map*, for the subsequent non-rigid registration with the intra-operative range-based surface. This is simply the Fast Marching method applied not to computing a distance map from the evolving $\{\Psi(X,t) = 0\}$ isosurface within a narrow band, but to computing distance and closest point label from the final brain surface everywhere in the volume. *As a result of its propagative nature* [47], *the FM algorithm is easily modified not only to estimate the distance of a surface to any voxel in the image volume, but also to store the identity of the particular surface point which is closest*. The motivation for using the FM algorithm is its computational efficiency and adaptability for storing Closest Point labels. However, there exist other methods for estimating distances which could serve the same purpose.

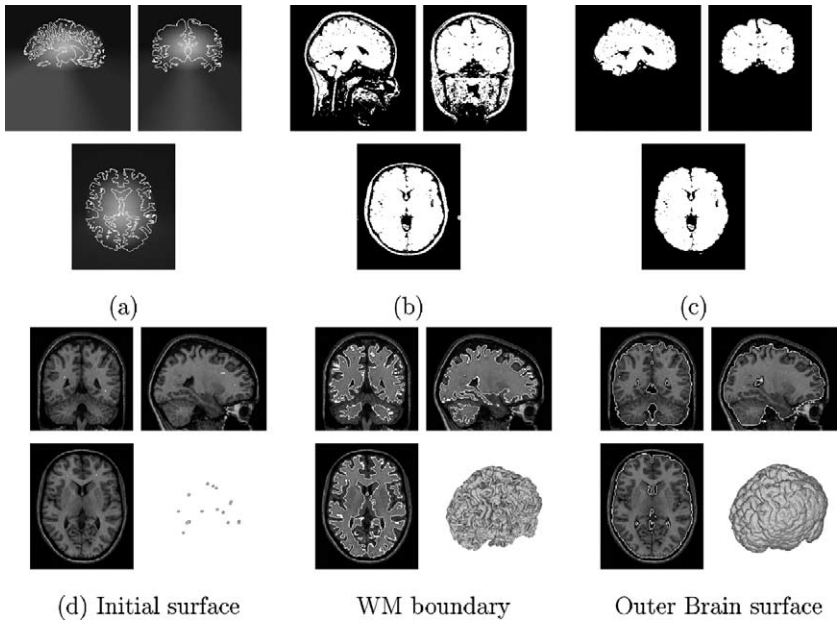

Fig. 7. WM/GM surface coupling: (a) WDF mapped to a grey-level intensity with WM contours in white; (b) speed function based on WM or GM tissue classes from T1 alone; (c) speed function, as in (b), but excluding GM voxels exceeding WDF shown in (a). (d) Surface model applied to ICBM subject 00100.

3. Validation and discussion

3.1. Validation of the range–MR transformation procedure

Validation of all procedures involved in relating range to MR is based on the skin phantom shown in Fig. 8a. This phantom features 12 glued-on torus-shaped fiducials, which are visible under both CT and MR. We opted for a CT validation, because the phantom contains metal wire in its core. The dimensions of the CT voxels are 0.89 mm in the x and y directions, and 1 mm in z. The localizing device used in this study is a FARO arm [58], discussed in Section 1. The overall range–CT transformation makes use of the prior IGS probe–CT transformation based on seven pairs of fiducials $\{\mathbf{x}^C_{F,k} \leftrightarrow \mathbf{x}^P_{F,k}\}$ accessible in probe space. The IGS transformation results for the left and right side studies are characterized by errors of 1.4 and 1.6 mm, respectively. The validation study consists of a comparison of

- *computed CT fiducial positions*: manually identified fiducials in the range image, transformed to CT space with the procedure presented here, against
- *manually identified fiducial positions in CT*.

While an automatic localization of the fiducials in both spaces may have been desirable, to do so reliably was difficult to achieve, due to self-occlusion in the range data.

Table 1 sums up the average values for disparities between identified and computed fiducial positions in CT space for the left and right side studies. Also featured in Table 1 is a description of the magnitude of the transformation between the two sensor base positions at t_c and at t_0 (during validation), from side-plate probe measurements. The transformation is expressed as two values: the magnitude of the calibration-OR translation vector $\|\mathbf{t}_c^0\|$ in mm and the angle of rotation θ_c^0 in degrees, about the rotation axis.[3]

These results are encouraging and they are consistent with the localization technology used for implementing the IGS registration. In particular, Rohling et al. [44] noted that the FARO estimates distances to within .5 mm, whereas the Optotrak is generally within 0.15 mm, and Alp et al. [2] have shown that torus-shaped fiducials are identified less precisely than other fiducials. Nevertheless, the goal of this procedure should be to achieve a characterization of the range–MR transformation to the nearest millimeter.

These results can be interpreted in the context of the formal relationship between the *fiducial localization error* (FLE) and the *target registration error* (TRE) explored by Maurer, Fitzpatrick et al. [38]. A lower bound on the final TRE of the calibration and sensor base tracking procedure can be estimated on the basis of the FLE or TRE associated with each step. Assuming a unity TRE $\approx$ TLE relationship (for the sake of simplicity), a probe FLE_P of 0.5 mm [44], and a range $\mathrm{FLE}_R \approx \sqrt{(0.5^2 + 0.5^2 + 0.5^2)} = 0.86$ mm, where a value of 0.5 mm is also presumed for the y-axis (due to limitations of the linear positioner calibration procedure), we assess the accuracy of the calibration plate localization as $\sqrt{(0.5^2 + 0.86^2)} \approx 1.0$ mm. The accuracy with which the sensor base divots can be located with respect to the range reference at t_c, is then $\sqrt{(1.0^2 + 0.5^2)} \approx 1.12$ mm. The accuracy of the sensor base tracking procedure, from t_c to t_0, is given by:

$$\mathrm{TRE}_{R\text{–}P,t_0} \approx \mathrm{FLE}_{\mathrm{tot},p_B} \approx \sqrt{(1.12^2 + 0.5^2)} \approx 1.22\,\mathrm{mm}. \tag{11}$$

If one factors in the TRE of the probe–CT transformation, which for this study is in the 1.5 mm range, then a reasonable lower bound for the final TRE is

$$\mathrm{TRE}_{R\text{–}M,t_0} = \sqrt{(\mathrm{TRE}_{R\text{–}P,t_0}^2 + \mathrm{TRE}_{P\text{–}M}^2)} \approx \sqrt{(1.22^2 + 1.5^2)} \approx 1.93\,\mathrm{mm}. \tag{12}$$

This value is compatible with the values observed in Table 1, particularly for a torus-shaped fiducial. Further analysis of these results indicates that the accuracy of the registration does not improve appreciably with robust statistics or with a subsequent skin-based ICP registration, and that there does not appear to be a correlation between the registration error and the size of the transformation [5]. The former finding suggests that the homologous pairs appear to preclude a severe outlier, as well as underscores the importance of their geometric configuration [38], since the systematic removal of information by the robust method tends to makes the registration degrade. The latter finding is consistent with most of registration error being

[3] Recall that a rotation can be expressed in terms Euler Symmetric Parameters, i.e., as an axis of rotation (k_x, k_y, k_z) and an angle of rotation θ about this axis (see [17, pp. 55–56]).

Table 1
Trial results for calibration and sensor base tracking procedure

$\|\mathbf{t}_{cal}^{OR}\|$ (mm)/θ_{cal}^{OR} (deg)		Trial 1	Trial 2	Trial 3	Trial 4	Trial 5
		293.4/ 11.0	139.1/ 11.1	201.6/ 12.9	265.5/ 53.8	167.0/ 14.4
Left side study						
Least squares	ϵ_{rms} (mm)	2.48	2.48	2.98	2.57	1.99
	d_{surf} (mm)	0.97	0.88	0.99	0.79	0.61
Robust	ϵ_{rms} (mm)	2.01	2.41	4.31	2.69	1.74
	d_{surf} (mm)	0.91	0.91	1.53	1.01	0.67
Least squares, ICP	ϵ_{rms} (mm)	2.44	2.47	2.71	2.57	2.09
	d_{surf} (mm)	0.46	0.47	0.47	0.47	0.46
Robust, ICP	ϵ_{rms} (mm)	2.11	2.16	3.90	2.51	2.01
	d_{surf} (mm)	0.46	0.46	0.49	0.46	0.45
		266.7/ 1.5	141.9/ 1.0	231.1/2.7	243.5/ 43.8	191.2/ 24.4
Right side study						
Least squares	ϵ_{rms} (mm)	2.14	2.48	3.39	2.43	2.19
	d_{surf} (mm)	0.97	0.52	0.89	0.91	0.63
Robust	ϵ_{rms} (mm)	2.11	3.08	5.40	2.71	3.08
	d_{surf} (mm)	0.66	0.92	1.65	0.86	0.72
Least squares, ICP	ϵ_{rms} (mm)	2.12	2.12	2.92	2.33	2.13
	d_{surf} (mm)	0.41	0.41	0.45	0.42	0.41
Robust, ICP	ϵ_{rms} (mm)	2.20	2.49	4.27	2.42	2.78
	d_{surf} (mm)	0.41	0.40	0.45	0.41	0.40

Rigid body transformation by least-squares and by robust regression, with and without ICP refinement based on the skin identified in CT and range spaces. The value ϵ_{rms} represents the RMS error (in mm) between CT fiducial positions and their homologues in the range image transformed to CT space by $\mathbf{T}_{range}^{CT}$. The value d_{surf} is the RMS distance (in mm) between the transformed range points and the CT skin surface. The symbols $\|\mathbf{t}_c^0\|$ and θ_c^0 indicate the magnitude of the translation and rotation between the sensor base positions at t_c and t_0.

tangential to the surface. One explanation could be a FLE in the range data which is more important than first thought. A pixel error of $(\delta i, \delta j)$ in the fiducial localization results in a localization error whose largest components are along x_R and y_R, for a brain surface which for all intents and purposes is normal to z_R.

3.2. Non-rigid registration validation: brain shift simulation by realistic elastic brain phantom

In order to assess non-rigid surface tracking, the set-screws under the phantom support plate are tightened, triggering a deformation of up to 15 mm at the top, and the phantom surface is then imaged by the range-sensor. A rough manual alignment

is provided, based on finding the points on the MR surface corresponding to the corners of the range domain and adding a vertical offset. The gradual improvement of the registration of the range and MR surfaces of the elastic phantom, over successive iterations and progressively more local characterization, can be illustrated as follows.

- *Distance statistics*: average and standard deviation values computed from the distance between homologous pairs, as shown in Fig. 9.
- *Spatial distribution of the distance between two surfaces*: this distance function can easily be visualized as a coloured point whose position is that of a surface point in range or MR space and whose colour is based on a distance-colour scale, as in Fig. 10. The top and bottom halves of this figure, respectively, illustrate the *forward* and *inverse transformation* results, including the rough manual starting point, the final rigid transformation, and the final non-rigid transformation.
- *2D slice illustration*: a qualitative illustration of the surface registration as it evolves over k and progressively more local characterization is provided by the consideration of any given 2D slice of the range image, such as shown for in Fig. 11 for the slice $y_R = 79.2$.

This section featured a new elastic brain-shaped phantom for physically replicating brain shift, and the ICP registration was validated on the basis of the distance between range and MR-based phantom surface. The results are consistent with other ICP registration papers, and with our objective of sub-mm surface registration. Our method features important efficiencies integrated in both the rigid and non-rigid stages, in the form of a Closest Point Map precomputation and the use of recursive splines. Despite some post-processing of the closest point pairs required to make the non-rigid transformation well defined, each iteration was virtually instantaneous.

One issue that we have not yet discussed is the accuracy of ICP techniques in recovering non-rigid motion, or in other words, the extent to which a small distance between two registered surfaces is a good predictor for recovering the actual non-rigid motion undergone by one of them. This issue is the subject of a validation study appearing in [5], whose results are summarized here for the sake of brevity. This study involves synthetic cortical range images, obtained by resampling top and left patches of the brain boundary of the Collins digital head phantom [14], to which an analytical deformation function is applied and compared with the estimated non-rigid motion. The conclusion of this study is that in general ICP techniques estimate non-rigid motion accurately (within 1 mm), but perform slightly less well in highly sloped areas, such as the deep recesses of sulci, where the closest point may not be the best homologue. This consideration may lead to a future refinement of our registration technique, in the same vein as the method of Feldmar and Ayache [19], where points which are both close in space and of similar surface shape would be considered homologous.

3.3. Surface model validation

The accuracy of our surface-based brain shift estimation framework presupposes an accurate brain segmentation algorithm. We have validated the brain surface iden-

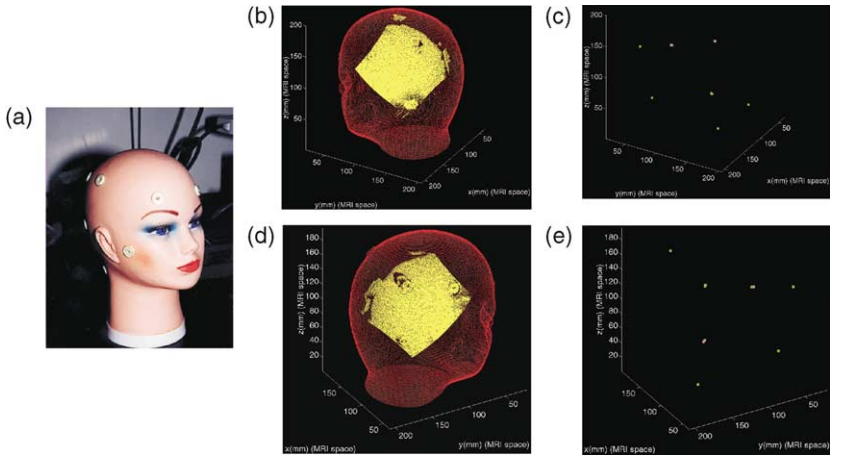

Fig. 8. (a) Skin phantom. Range–CT transformation results (trial 1): (b–c) left side: (b) range data transformed to CT space overlaid on CT data; (c) CT (green) and transformed range space (pink) fiducials; (d–e) right side: (d) transformed right side range data overlaid on CT data; (e) CT space and transformed range space fiducials.

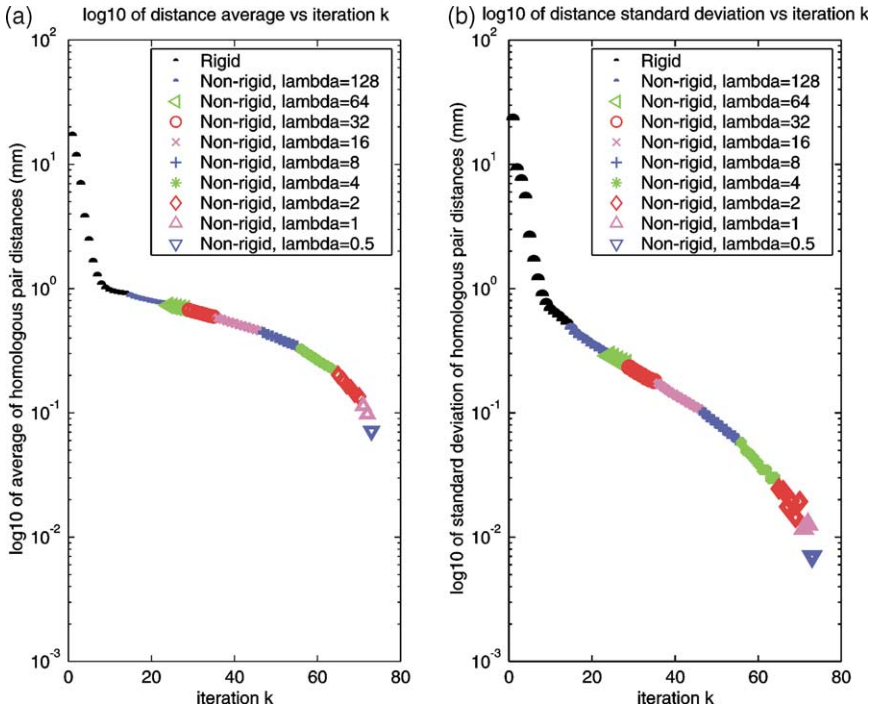

Fig. 9. Statistics of distances between homologous points, assuming an overall transformation $\mathbf{T}_R^M$ (based on expressions 4 evaluated up to iteration $K = k$ or $L = k$) applied to range points: (a) $\log_{10}$ of distance average; (b) $\log_{10}$ of distance standard deviation.

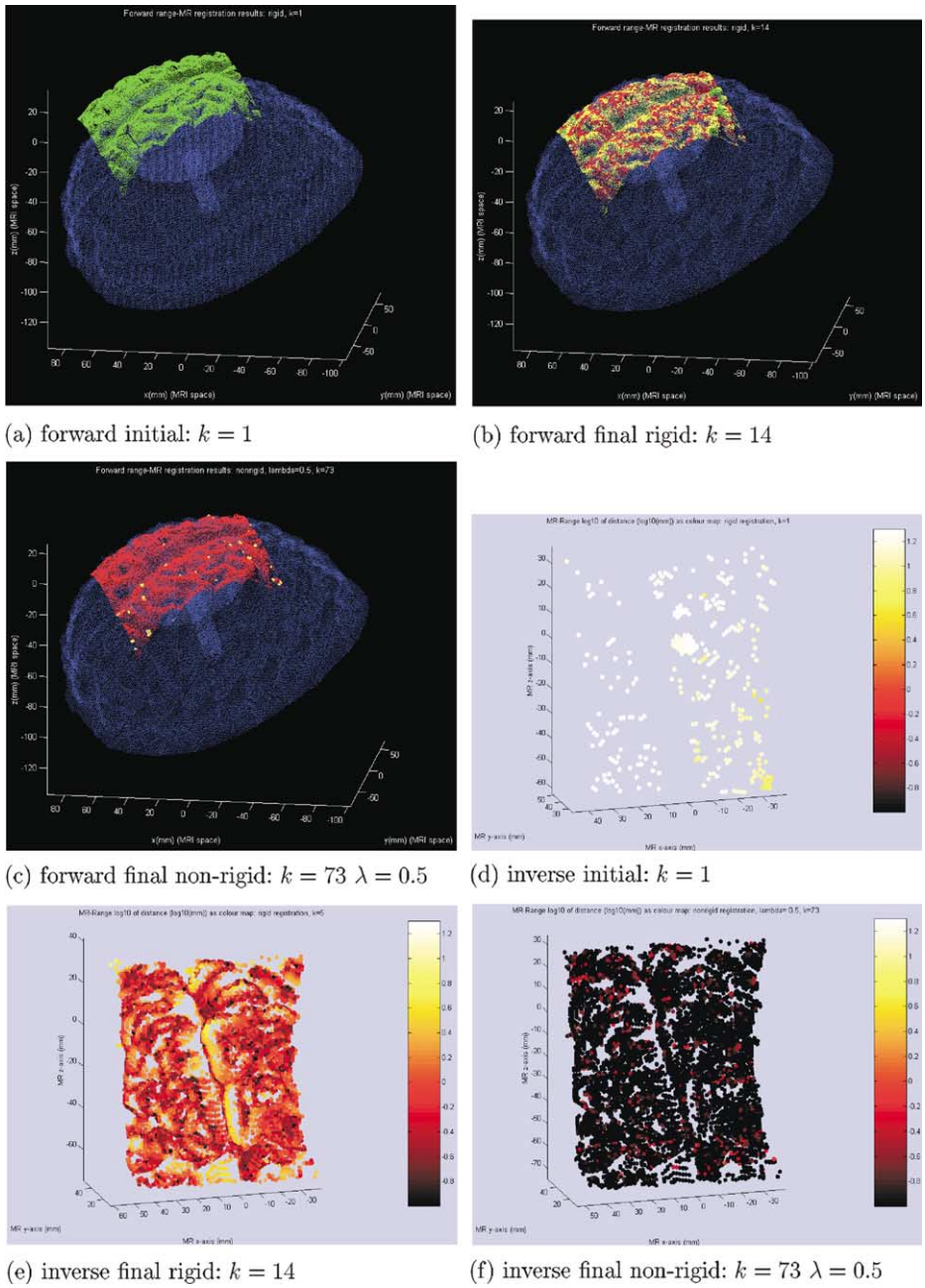

(a) forward initial: $k = 1$

(b) forward final rigid: $k = 14$

(c) forward final non-rigid: $k = 73$ $\lambda = 0.5$

(d) inverse initial: $k = 1$

(e) inverse final rigid: $k = 14$

(f) inverse final non-rigid: $k = 73$ $\lambda = 0.5$

Fig. 10. Forward and inverse transformation results, featuring initial, final rigid, and final non-rigid transformations. The colour scheme of the data indicates the distance between the range to MR brain surfaces. (a)–(c): Forward-transformed range data, red: $d < 0.5$ mm, yellow: $0.5 \leqslant d < 2.0$ mm, green: $d \geqslant 2.0$ mm. (d)–(f): Inverse-transformed MR data; logarithmic scale: black corresponds to -1.0 (0.1 mm), saturated red to -0.17 (0.67 mm), saturated yellow to 0.67 (4.78 mm), and white to 1.3 (20 mm).

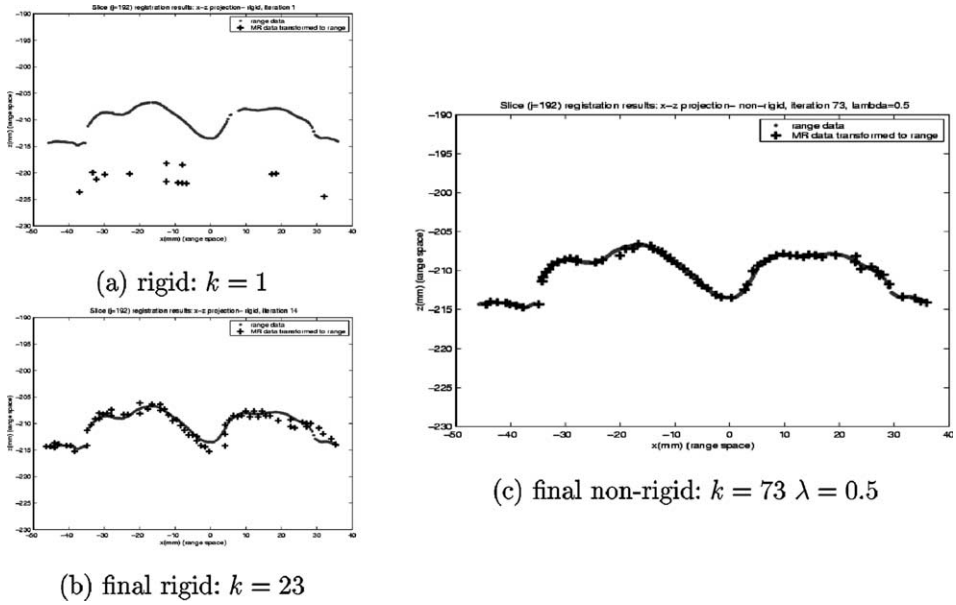

Fig. 11. Inverse transformation results, featuring initial, final rigid, and final non-rigid transformations, for the *slice* $y_R = 79.2$ ($j = 192$). Shown here are homologous range points and MR brain points mapped back to range space according to $\mathbf{T}^R_{M,k}$ and projected to the x_R–z_R plane.

tification technique presented so far with a quantitative approach based on realistic synthetic data, where ground truth is known, and qualitative tests with in vivo subject data. The latter data comes in the form of healthy subject scans obtained from the ICBM[4] database, as well as Montreal Neurological Institute (MNI) patient scans featuring pathologies and this qualitative validation is presented in [5].

The quantitative validation stage presented in this section makes use of two software tools which were developed at the MNI: a MRI simulator specifically designed and implemented by Kwan et al. [29] for the purpose of image analysis evaluation, and a high-resolution, volumetric, anthropomorphic digital brain phantom elaborated by Collins et al. [14]. In turn, the healthy-subject digital phantom is the starting point for a second phantom featuring pathological tissue [10]. The accuracy of the segmentation of the brain surface within simulated T1-weighted MR data can be assessed from the known boundary of the brain within the digital phantom, as shown in Fig. 12 (for more details see [5]).

The evolution of the zero-level isosurface, from spheres imbedded in white matter, through the white matter boundary, to the outer brain surface, is illustrated for healthy subject 00100 from the ICBM database in Fig. 7. This example represents the worse case, from a classification standpoint: T1 data considered alone, as one

[4] International Brain Mapping Consortium.

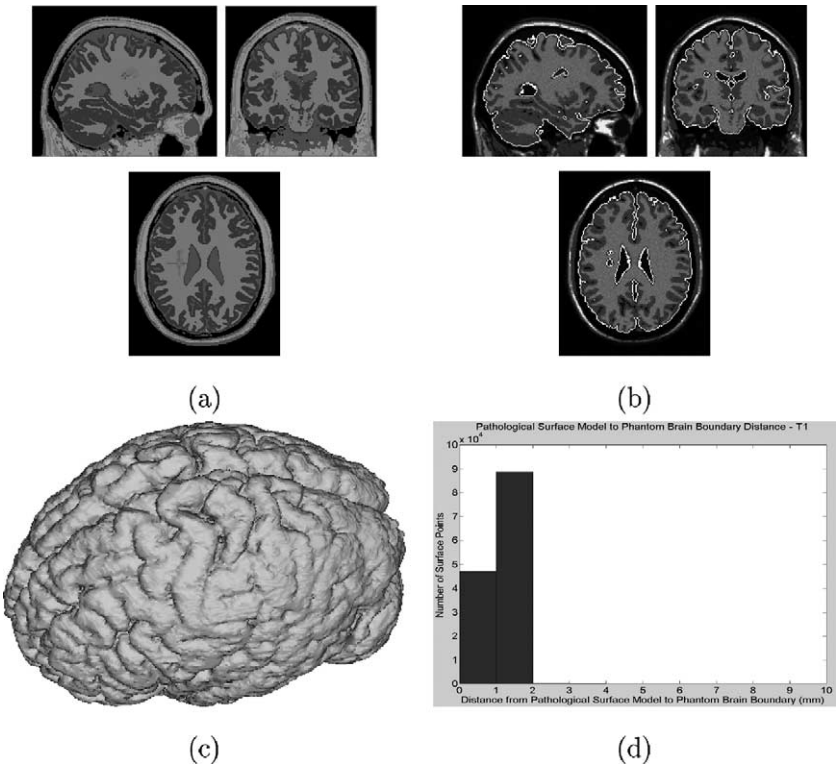

Fig. 12. Surface model behaviour with synthetic pathological data: (a) original pathological phantom and (b)–(e) brain surface identified with surface model, from simulated T1-weighted scan; (b) tri-planar view; (c) rendered view; (d) distribution of distance between brain surface in scan and phantom brain boundary: avg. $= 0.68 \pm 0.51$ mm.

would expect the tissue discrimination ability of the classifier to improve with the consideration of T2- and PD-weighted data.

This section presented a brief overview of the validation study of our surface evolution model. Our study makes use of data from real subjects both healthy and with pathologies, as well as synthetic data both with and without simulated pathological tissue. One point not discussed so far is that the model as currently implemented assumes a voxel-based boundary, in particular because the FM technique employed at the time used a voxel-based surface as a starting point. However, FM techniques for triangulated surfaces have since been published, and it should be feasible to adapt the Closest Point Map computation to triangulated surfaces as well. This improvement would be significant, as it would produce a Distance and Closest Point Map of a surface established with sub-voxel accuracy. The overall accuracy of the surface tracking method proposed here is dependent on the accuracy of all its constituent stages, so that an overall objective of 1 mm presupposes segmentation accuracy well within 1 mm, which in turn will probably only accrue from a sub-voxel, triangulated method.

4. Conclusion

This paper addressed the problem of intra-surgical brain deformation, and suggested a non-rigid surface registration framework for characterizing this deformation. The objective of this framework was to produce a smoothed, dense vector displacement function from the undeformed preoperative brain surface, semi-automatically identified in MR data, to the exposed intra-operative brain surface characterized with a laser range-sensor and referred to the MR coordinate system. This vector displacement function could then be interpolated everywhere in the brain volume, on the basis of an ulterior volumetric, constitutively realistic FE model.

Furthermore, the methods proposed here were conceived from assumptions based on practical clinical requirements. First, the semi-automatic method for identifying the brain surface in MR should be able to cope with the presence of imdedded pathology, even very large tumours. Next, the 3D surface capture and surface registration methods should be fast, producing results virtually at the instant they are required in the OR, with no user intervention except to initiate the processes. And finally, the method for relating the MR and range spaces must function despite the presence of large swaths of surgical draping, possibly occluding one or more intra-surgical fiducials, which suggests a calibration-based solution.

The underlying assumption of this paper is that an accurate volumetric displacement characterization is possible with a displacement map at the exposed cortical surface and with a suitable finite-element model. The documented use of volumetric FE models, with sparse surface displacement data and with surface models fit to intra-operative MR data, suggests that at the very least, the accurate volumetric estimation of intra-surgical brain displacement with this framework is highly feasible. A future validation study which would support this hypothesis is the comparison of the position of beads imbedded in our elastic brain-shaped phantom, as detected within a MR volume, against the position predicted on the basis of a surface registration and volumetric interpolation approach. Furthermore, the method presented here is entirely compatible with the integration of probe-based information about the volume of resected tissue [48], whose interaction with the finite-element brain model could be inspired from cutting models used in surgical simulation [33].

References

[1] D. Adelsteinsson, J.A. Sethian, A fast level set method for propagating interfaces, J. Comput. Phys. (118) (1995) 269–277.
[2] M.S. Alp et al., Head registration techniques for image-guided surgery, Neurol. Res. 20 (1998) 31–37.
[3] K.S. Arun, T.S. Huang, S.D. Blostein, Least-squares fitting of two 3-D point sets, IEEE Trans. PAMI 9 (5) (1987) 698–700.
[4] M.A. Audette, F.P. Ferrie, T.M. Peters, An algorithmic overview of surface registration techniques for medical imaging, Med. Imag. Anal. 4 (3) (2002) 201–217.
[5] M.A. Audette, Surface-based characterization of intra-surgical brain deformations in image-guided surgery, Ph.D. thesis, Dept. Biomedical Engineering, McGill University, Montreal, Canada, 2002.
[6] M.A. Audette, Global structure-preserving voxel classification for patient-specific surgical simulation, Proc. IEEE Conf. EMBS Houston, 2002.

[7] www.barebonesstore.com/products/default.asp?Prod = 86.
[8] P.J. Besl, N.D. McKay, A method for registration of 3-D shapes, IEEE Trans. Pattern Anal. Mach. Intell. 14 (2) (1992) 239–256.
[9] F. Blais, J.A. Beraldin, Calibration of an anamorphic laser based 3-D range sensor, SPIE Proc. Videometrics V 3174 (1997) 113–122.
[10] P.A. Bottomley et al., A review of ^{1}H nuclear magnetic resonance relaxation in pathology: are T_1 and T_2 diagnostic?, Med. Phys. 14 (1) (1987) 1–37.
[11] R.J. Campbell, P.J. Flynn, Eigenshapes for 3D object recognition in range data, Proc. IEEE Conf. Computer Vision & Pattern Recognition (1999).
[12] V. Caselles, et al., Minimal surfaces: a three dimensional segmentation approach, Technion EE Pub. No. 973, 1995.
[13] K.C. Chu, B.K. Rutt, Polyvinyl alcohol cryogel: an ideal phantom material for MR studies of arterial flow and elasticity, Magn. Reson. Med. (37) (1997) 314–319.
[14] D.L. Collins et al., Design and construction of a realistic digital brain phantom, IEEE Trans. Med. Imaging 17 (3) (1998) 463–468.
[15] R.M. Comeau, Intraoperative ultrasound imaging for the detection and correction of tissue movement in image-guided surgery, Ph.D. Thesis, Dept. Biomedical Engineering, McGill University, Montreal, 2000.
[16] R.M. Comeau et al., Intra-operative ultrasound for guidance and tissue shift correction in image-guided neurosurgery, Med. Phys. 27 (4) (2000).
[17] J.J. Craig, Introduction to Robotics: Mechanics and Control, Addison-Wesley, Reading, MA, 1989.
[18] R.O. Duda, P.E. Hart, Pattern Analysis and Scene Analysis, Wiley/Interscience, New York, 1973.
[19] J. Feldmar, N. Ayache, Rigid and affine registration of free-form surfaces, using differential properties, Proc. Eur. Conf. Comp. Vision (1994) 397–406.
[20] M. Ferrant et al., Registration of 3D intra-operative MR images of the brain using a finite element biomechanical model, MICCAI (2000) 19–27.
[21] R.L. Galloway, R.J. Maciunas, J.W. Latimer, The accuracies of four stereotactic frame systems: an independent assessment, Biomed. Instr. Tech. 2 (1991) 457–460.
[22] A. Guéziec, N. Ayache, Smoothing and matching of 3-D space curves, Internat. J. Comp. Vision 12 (1) (1994) 79–104.
[23] Intelligent Actuator (IAI), www.intelligentactuator.com.
[24] ISG Technologies Inc., Viewing Wand Image-Guided Surgical System- Operator's Guide, 1997.
[25] A.E. Johnson, M. Hebert, Surface matching for object recognition in complex three-dimensional scenes, Image Vision Comput. 16 (1998) 635–651.
[26] M. Kass, A. Witkin, D. Terzopoulos, Snakes: active contour models, Internat. J. Comput. Vision 2 (1987) 321–331.
[27] P.J. Kelly et al., Computer-assisted stereotaxic laser resection of intra-axial brain neoplasms, J. Neurosurg. (64) (1986) 427–439.
[28] R. Khadem et al., Comparative tracking error analysis of five different optical tracking systems, Comput. Aided Surg. 5 (2000) 98–107.
[29] R.K.-S. Kwan, A.C. Evans, G.B. Pike, MRI simulation-based evaluation of image-processing and classification methods, IEEE Trans. Med. Image Anal. 18 (11) (1999).
[30] S. Lavallée, R. Szeliski, Recovering the position and orientation of free-form objects from image contours using 3D distance maps, IEEE Trans. Pattern Anal. Mach. Intell. 17 (4) (1995) 378–390.
[31] W.E. Lorensen, H.E. Cline, Marching cubes: a high resolution 3D surface construction algorithm, Comput. Graph. 21 (3) (1987) 163–169.
[32] D. MacDonald, D. Avis, A.C. Evans, Proximity constraints in deformable models for cortical surface identification, Med. Image Comput. Comput.-Assisted Intervention—MICCAI'98 (1998) 650–659.
[33] M. Mahvash, V. Hayward, Haptic rendering of cutting: a fracture mechanics approach, www.Haptics-e.org 2(3).
[34] R. Malladi, J.A. Sethian, B.C. Vemuri, Shape modeling with front propagation: a level set approach, IEEE Trans. Pattern Anal. Mach. Intell. 17 (2) (1995).

[35] D. Marr, Vision, W.H. Freeman & Co., 1982.
[36] C.R. Maurer et al., Measurement of intra-operative brain deformation using a 1.5 Tesla interventional MR system: preliminary results, IEEE Trans. Med. Imag. 17 (5) (1998) 817–825.
[37] C.R. Maurer et al., Measurement of intra-operative brain surface deformation under a craneotomy, Medical Image Computing and Computer-Assisted Intervention MICCAI (1998) 51–62.
[38] C.R. Maurer et al., Registration of head volume images using implantable fiducial markers, IEEE Trans. Med. Imag. 16 (4) (1997).
[39] J. Michiels et al., On the problem of geometric distortion in magnetic resonance images for stereotactic neurosurgery, Magn. Reson. Imag. 12 (5) (1994) 749–765.
[40] M.I. Miga et al., Updated neuroimaging using intra-operative brain modeling and sparse data, Stereotac. Func. Neurosurg. 72 (1999) 103–106.
[41] J. Montagnat et al., Representation, shape, topology and evolution of deformable surfaces. Application to 3D medical segmentation, Image Vision Comput. 19 (14) (2001) 1023–1040.
[42] Northern Digital Inc., www.ndigital.com.
[43] A. Olivier et al., Image-guided surgery of epilepsy, in: R.J. Maciunas (Ed.), Clinical Frontiers of Interactive Image-Guided Neurosurgery, Neurosurg. Clin. North Am. 7 (2) (1996) 245–266.
[44] R. Rohling et al., Comparison of relative accuracy between a mechanical and an optical position tracker for image-guided neurosurgery, J. Imag. Guid. Surg. 1 (1995) 30–34.
[45] A. Rosenfeld, A.C. Kak, Digital Picture Processing, second ed., Academic Press, New York, 1982.
[46] H. Schiffbauer, Neuronavigation in brain tumor surgery-clinical beta-phase of the Oulu Neuronavigator System, Academic Dissertation, Faculty of Medicine, Univ. Münster, available online at http://herkules.oulu.fi/isbn9514252543.
[47] J.A. Sethian, Fast marching level set method for monotonically advancing fronts, Proc. Natl. Acad. Sci. USA 93 (1996) 1591–1595.
[48] M. Sinasac, Use of 3D deformable models for intra-operative visualization and quantification of cerebral tissue resection, Master's Thesis, Dept. Electrical and Computer Engineering, McGill University, 1999.
[49] O. Škrinjar, D. Spencer, J. Duncan, Brain shift modeling for use in neurosurgery, MICCAI (1998) 641–649.
[50] R. Szeliski, S. Lavallee, Matching 3-D anatomical surfaces with non-rigid deformations using octree-splines, Internat. J. Comput. Vision 182 (1996) 171–186.
[51] D. Terzopoulos, D. Metaxas, Dynamic 3D models with local and global deformations: deformable superquadrics, IEEE Trans. Pattern Anal. Mach. Intell. 13 (7) (1991) 703–714.
[52] J.-Ph. Thirion, Extremal points: definition and application for 3D image registration, Proc. IEEE Conf. Computer Vision and Pattern Recognition (1994) 587–592.
[53] M. Unser, A. Aldroubi, M. Eden, B-spline signal processing: part I-theory, IEEE Trans. Signal Proc. 41 (2) (1993) 821–833.
[54] Vitana Corporation, ShapeGrabber Reference Manual, 1997.
[55] M.Y. Wang et al., An automatic technique for finding and localizing externally attached markers in CT and MR volume images of the head, IEEE Trans. Biomed. Eng. 43 (6) (1996).
[56] X. Zeng et al., Segmentation and measurements of the cortex from 3D MR images, Med. Image Comput. Comput.-Assisted Intervention—MICCAI'98 (1998) 519–530.
[57] C. Zhou, T.B. Khalil, A.I. King, A New Model Comparing Impact Responses of the Homogeneous and Inhomogeneous Human Brain, Society of Automotive Engineers, Inc. report #952714, 1995.
[58] S.J. Zinreich et al., Frameless stereotaxic integration of CT imaging data: accuracy and initial applications, Radiol. 188 (3) (1993) 735–742.